

**On the local corrosion behavior of coupled welded zones of the 2098-T351 Al-Cu-Li alloy produced by Friction Stir Welding (FSW): An amperometric and potentiometric microelectrochemical investigation.**

Rejane Maria P. da Silva<sup>1,2</sup>; Javier Izquierdo<sup>2,3</sup>; Mariana X. Milagre<sup>1</sup>; Abenchara María Betancor-Abreu<sup>2</sup>; Leandro A. de Oliveira<sup>4</sup>; Renato A. Antunes<sup>4</sup>; Ricardo M. Souto<sup>2,3</sup>; Isolda Costa<sup>1</sup>

<sup>1</sup> *Instituto de Pesquisas Energéticas e Nucleares - IPEN/CNEN - Av. Prof. Lineu Prestes, 2242 - São Paulo, Brazil*

<sup>2</sup> *Department of Chemistry, Universidad de La Laguna, P.O. Box 456, E-38200 La Laguna (Tenerife), Canary Islands, Spain*

<sup>3</sup> *Institute of Material Science and Nanotechnology, Universidad de La Laguna, P.O. Box 456, E-38200 La Laguna (Tenerife), Canary Islands, Spain.*

<sup>4</sup> *Centro de Engenharia, Modelagem e Ciências Sociais Aplicadas (CECS), Universidade Federal do ABC (UFABC), Av. dos Estados 5001, 09210-580 Santo André, SP, Brazil.*

**Abstract**

The galvanic coupling effects and the local electrochemical activity developed along the welded zones in FSWelded 2098-T351 Al-Cu-Li alloy have been investigated using localized electrochemical methods supported by surface analytical characterizations. The investigation was carried out in the coupled welding joint/heat affected zones (WJ/HAZ) for both the retreating (RS) and the advancing (AS) sides. The correlation between surface chemistry, microstructural features and electrochemical activity of these welded zones has been studied. The results showed the development of galvanic interactions within and between the WJ and the HAZ regions that were visualized using the Scanning vibrating electrode technique (SVET) and scanning electrochemical microscopy (SECM). SVET analyses showed that the HAZ was more susceptible to the development of anodic sites compared to WJ. SECM in amperometric operation mode showed that the WJ coupled to HAZ presented higher oxygen consumption and greater cathodic activity compared to HAZ. Furthermore, SECM in the potentiometric operation mode showed alkalization on the WJ and increased acidity on the HAZ, mainly at severe localized corrosion (SLC) sites. Based on SVET and SECM results in combination surface analysis, it is proposed that the micro-galvanic cells formed

within these welded zones are due to the presence of secondary phases in the 2098-T351 alloy and their interactions with the adjacent matrix.

**Keywords:** Al-Cu-Li alloys; Friction stir welding; galvanic coupling effects; Local electrochemical activity; SVET; SECM.

## 1. Introduction

Al-Cu-Li alloys are being developed for aerospace applications due to their higher specific strength compared to conventional Al-alloys. The addition of Li to these alloys reduces its density and increases its mechanical strength [1,2]. Weight reduction makes its application in aircraft structures attractive, decreasing fuel consumption. However, Li additions also increase the susceptibility of Al-Cu alloys to localized corrosion reactions [3,4], a characteristic that is enhanced by welding. In fact, welding processes are responsible for microstructural changes in the welded joint resulting in macro-galvanic coupling and corrosion susceptibility in the different zones after welding [5-7].

Friction stir welding (FSW) has great potential as welding process for Al-alloys. It is a solid-state process that can be applied for materials that are difficult to weld using conventional processes as it is the case of Al alloys. This type of welding modifies the microstructure of the parent material through mechanical and thermal effects, resulting in the formation of various zones that present different microstructures [5,8]. Changes in microstructural features due to the FSW process have been described in the literature [9-11]. The high temperatures reached and the intense plastic deformation in the welding joint (WJ) lead to the formation of a thermo-mechanically affected zone (TMAZ) and a stir zone (SZ). Next, thermal effects also allow differentiation of the heat-affected zone (HAZ) from the unaffected parent metal (PM) [12-14]. Moreover, due to the differences in the material flow and the heat transfer on both sides of the weldment, the two sides of the joint present different microstructural features [15-18]. Thus, in the retreating side (RS), the directions of transverse motion and tangential vector of the tool rotation speed are in opposite directions, whereas in the advancing side (AS), they are in the same direction [1-4]. Additionally, material transport occurs from the RS to the AS sides [19].

Differences in the corrosion behavior of the RS and the AS have been reported in the literature for various Al-alloys [15-17]. When studying the 7020 Al-alloy welded by FSW, Dudzik observed that the RS was more susceptible to corrosion compared to the AS [15].

Another work showed that the unequal distribution and clustering of coarse intermetallic particles across the different zones of the welded joint in FSWelded 2024-T3 Al-alloy was responsible for distinct electrochemical activities along the material. Clusters of coarse intermetallic particles were more evident in the TMAZ of the RS, resulting in the greater susceptibility of this zone to localized corrosion [17]. More recently, Milagre et al. [19] showed the influence of asymmetry effects from the FSW process on the localized corrosion susceptibility of the 2098-T351 Al-Cu-Li alloy welded by FSW, and they reported that the electrochemical activity was higher in the RS compared to the AS.

The 2098 Al-Cu-Li alloy is a 3<sup>rd</sup> generation Al-Li alloy [20] that was produced as a potential substitute for conventional Al-alloys of the 2XXX series [21]. This alloy contains Cu, Li, Mg, Ag, Zr, Si, and Fe in its composition, which is responsible for its advanced microstructure and the precipitation of hardening phases such as T1 (Al<sub>2</sub>CuLi), which is described as the main strengthening phase in the new generation Al-Cu-Li alloys [22]. The T1 phase is reported to be highly active due to the presence of Li, and its fast selective dissolution leads to Cu-enrichment, polarity reversal and, subsequently, dissolution of the Al matrix, in aggressive environments [1,3,23]. However, the amount and morphology of this phase are modified by the FSW process [19], while causing distinct degrees of thermal gradients and mechanical deformation [5,8].

High corrosion activities for various Al-Cu-Li alloys welded by FSW have been reported [5-8,24-27]. Among them, recent investigations by our group on the related AA2198 Al-Cu-Li alloy have shown that the parent material (PM) region is the most susceptible to localized corrosion in Al-Cu-Li alloys welded by FSW, a feature due to the highest amount of the T1 phase occurring in this region [6,7,27]. Conversely, higher resistance to localized corrosion was observed in the SZ, where the T1 phase is scarce. Unfortunately, although it is agreed that Al-Cu-Li alloys are highly susceptible to localized corrosion activity, controversy exists in the scientific literature concerning the localized distribution of corrosion processes along the FSW material [4,5,8,24,25]. For instance, Corral et al. [24] reported similar current densities and corrosion potentials for the FSW zone and PM region of 2195 Al-alloy. Even more scarce are the reports on the corrosion behavior of the 2098 Al-Cu-Li alloy [28-30]. In addition, few attempts have been made to investigate these localized processes using localized electrochemical techniques [19,31], although the applicability of localized electrochemical techniques for the investigation of the corrosion activity of some Al-Cu-Li alloys has been reported in the literature [7,29,30,32]. Thus, scanning probe techniques with

electrochemical selectivity, such as the scanning vibrating electrode technique (SVET), scanning electrochemical microscopy (SECM) and the local electrochemical impedance spectroscopy (LEIS), were employed to study galvanic coupling effects on the local electrochemical activity due to the different zones in contact in dissimilar Al-alloys welded by FSW, namely for the 7050/2024 [33], 2024/7475 [34], and 2050/7449 systems [35]. In those works, these localized electrochemical techniques were shown useful to evaluate the local electrochemical response in the different zones resulting from FSW of different Al-alloys. More recently, local electrochemical differences resulting from FSW when joining the same material were shown by Donatus et al. in the case of 2198-T851 Al-Cu-Li alloy using SECM technique [27]. In this study, the authors reported that the PM was the most anodic zone compared to others regions of the welded alloy, and developed severe localized corrosion (SLC) sites.

The main purpose of this work was study the galvanic coupling effects and local electrochemical activity of the welding zones interfaces of the FSWelded 2098-T351 Al-Cu-Li alloy. In this study, surface chemistry and microstructural features were correlated to electrochemical activity of the welded zones interfaces. Electrochemical studies were carried out in the coupled welding WJ/HAZ (in both RS and AS cases) zones using potentiodynamic polarization and scanning electrochemical techniques (namely, SVET and SECM in amperometric and potentiometric operation modes). SECM in the amperometric operation mode has already been employed to characterize different Al-alloys [35-39], whereas potentiometric probes have been shown to be interesting tools in corrosion studies, particularly for the investigation of other galvanic corrosion effects [40-43]. But to the best of the authors knowledge, the combined use of amperometric and potentiometric SECM probes to investigate different regions of Al-Cu-Li alloys welded by FSW has not been reported in literature.

## **2. Experimental**

### *2.1 Materials*

Samples of a 2098-T351 alloy (3.4 wt% Cu, 1 wt% Li, 0.3 wt% Mg, 0.3 %wt Ag, 0.4 wt% Zr, 0.04 wt% Fe, 0.05 wt% Si, 0.02 wt% Zn, 0.003 wt% Mn) welded by friction stir welding (FSW) were used in this work. The FSW process was performed using a transverse speed of 150 mm/min and a rotation rate of 1000 rpm. The diameter of the tool shoulder was 10 mm while that of the pin was 5 mm. All measurements were performed on the top surface of the

FSW alloy. For that purpose, each sample was embedded in *Epofix* epoxy resin (Struers, Ballerup, Denmark) to produce a disk-shaped resin mount (dia. 3 cm), and cured for 24 h at ambient temperature. The top side of the mount with the sample at its center was abraded sequentially with #500, #800, #1500, #2500 and #4000 grit carbide silicon papers, and polished with diamond suspensions of 3  $\mu\text{m}$  and 1  $\mu\text{m}$ .

## *2.2 Microstructural and surface characterization*

Optical microscopy was employed for surface observation after etching the surfaces in a solution with 2% (v/v) HF and 25% (v/v)  $\text{HNO}_3$  in deionized water. Optical micrographs of the samples were also obtained after immersion in naturally-aerated 5 mmol/L NaCl solution for 24 h at room temperature ( $22 \pm 2$  °C). Vickers microhardness tests were carried out at the top surface of the FSWelded 2098-T351 alloy in successive steps of approximately 0.3 mm with a load of 0.3 g for 10 s of dwell time, using a HM-101 Mitutoyo Microhardness tester (Neuss, Germany). A scanning electron microscope (SEM, ZEISS EVO 15, White Plains, NY, USA) equipped with X-ray dispersive energy microanalyzer (EDX, Oxford Instruments X-MAX system, High Wycombe, UK) was employed for the compositional analysis of micrometric particles occurring in the polished 2098-T351 alloy (both for parent material (PM) and for FSWelded samples).

The chemical composition of the surfaces was obtained by X-ray photoelectron spectroscopy (XPS) using a K-alpha<sup>+</sup> spectrometer (Thermo Fisher Scientific, Waltham, MS, USA). The beam was generated by a monochromatic Al K- $\alpha$  radiation source. The pressure in the analysis chamber was approximately  $10^{-7}$  Pa. High resolution spectra of the polished FSWelded 2098-T351 alloy were acquired before and after exposure to 5 mmol/L NaCl aqueous solution for 72 h.

Gel visualization tests were performed in order to observe the anodic and cathodic zones developed on the 2098-T351 alloy welded by FSW. The gel was prepared using 100 mL of a boiling solution with 0.6 mol/L of NaCl. 3 g of agar-agar and 7 mL of universal indicator were added to this solution. Subsequently, the gel was poured over the polished surfaces, and the development of features due to corrosion was monitored as a function of time at room temperature ( $22 \pm 2$  °C).

## *2.3 Electrochemical characterization*

Potentiodynamic polarization tests were specifically performed on different regions of the welded joint in the FSW 2098-T351 samples by using an electrochemical cell that limited approximately 0.20 cm<sup>2</sup> of the alloy. They were carried out using a Solartron 1287 potentiostat (Leicester, UK) in a conventional 3-electrode configuration, with a platinum wire as the auxiliary electrode, Ag/AgCl/KCl(sat) as reference electrode, and the FSW 2098-T351 sample as the working electrode. All potential values reported in this work are referred to the Ag/AgCl/KCl(sat) reference electrode. Polarization scans were carried out in naturally aerated 5 mmol/L NaCl solution at room temperature (22 ± 2 °C). The potential scans were recorded after 15 min exposure to the test solution in order to achieve a stable open circuit potential. They were initiated from a potential value 50 mV more negative than the corresponding OCP, and the potential was scanned in the positive direction up to +1.00 V with a scan rate of 0.5 mV/s.

SVET measurements were performed using an Applicable Electronics instrument (New Haven, CT, USA) controlled by *Automated Scanning Electrode Technique* (ASET) software. A vibrating probe of Pt-Ir was used after platinization, in order to generate a spherical platinum black deposit of 20 µm diameter at the tip. The frequency of the probe vibration was 190 Hz along the X axis, and 70 Hz along the Z axis, both with an amplitude of 20 µm. Scans were carried out over the 2098-T351 welded samples (embedded in epoxy resin) at a height of approximately 170 µm, established using the in-built video-imaging system provided with the equipment. The SVET scans were carried out in naturally aerated 5 mmol/L NaCl solution at ambient temperature (22 ± 2 °C) for 3 h. The investigated sample was left unpolarized, effectively at its open circuit potential.

High-resolution Sensolytics SECM equipment (Bochum, Germany), built around an Autolab (Metrohm, Herisau, Switzerland) electrochemical interface and controlled with a personal computer, was used in two different operation modes: amperometric and potentiometric, by using Pt and Sb microelectrodes, respectively. The experiments were performed in aerated 5 mmol/L NaCl solution at room temperature (22 ± 2 °C) for 3 h. The sample was not polarized during the measurements.

For amperometric measurements, a platinum microdisk of 10 µm diameter was employed. A Pt wire as counter electrode, and a Ag/AgCl/KCl(sat) reference electrode completed the small electrochemical cell. The amperometric tests were performed using the Redox Competition mode with the Pt probe biased at -0.70 V. This mode is related to the content of dissolved molecular oxygen in the test solution that is monitored from its electro-

reduction at the Pt probe. In this mode, the probe and the investigated surface compete for the oxygen contained in the solution [44]. Scans in the X-Y plane were carried out with the Pt-probe located at a height of approximately 20  $\mu\text{m}$  over the surface. To establish this working distance, a Z-approach curve was recorded above each region of the joint before measuring the corresponding SECM map. The redox competition mode was employed, and changes in the limiting current for the electro-reduction of dissolved oxygen were observed when the Pt probe approached the investigated surface [44,45].

The potentiometric SECM measurements were performed using a Sb microelectrode. For this purpose, micropipettes were molded by pulling borosilicate capillaries (wall thickness 0.225 mm, outer diameter  $\varnothing = 1.5$  mm, provided by Hilgenberg GmbH (Malsfeld, Germany), employing a model P-30 micropipette puller (Sutter Instrument, Novato, CA, USA). Subsequently, Cu wire (ca. 12 cm length and 0.5 mm diameter) and Sb fibre (2.0 cm length and approximately 15-20  $\mu\text{m}$  diameter) were used to fabricate the Sb microelectrode. The Sb fibre was inserted into the lumen of the micropipette with the tip protruding out for about 5 mm. The electrical contact of the Sb fibre and the Cu wire into the micropipette was obtained using a small quantity of liquid mercury metal. The two micropipette ends were sealed with *Loctite*<sup>®</sup> adhesive. More information on the fabrication of the Sb probe was given elsewhere [41]. In the measuring circuit, a voltage follower based on a  $10^{13}$  input impedance operational amplifier (mod. TL071, Texas Instruments, Dallas, TX, USA) was inserted. The pH response of the Sb probe was subsequently calibrated in a set of pH buffers. A linear relationship between the solution pH and the potential, with slope of -44 mV/pH unit, was obtained in the  $3 < \text{pH} \leq 11$  range. Next, the Sb probe was employed in combination with an Ag/AgCl/KCl(sat) reference electrode for the potentiometric SECM tests. The Sb probe was placed at a height of approximately 50  $\mu\text{m}$  above of the sample, adjusted with the help of a video camera TV system.

### **3. Results and Discussion**

#### *3.1 Surface characterization*

The microstructural features of the different FSW zones of the 2098-T351 Al-Cu-Li alloy can be observed from the inspection of the optical micrographs shown in [Figure 1](#). The micrographs of the top surface, Figure 1(a), and the cross-section, Figure 1(b), evidence the development of different microstructural features across the weldment as result of the FSW process. In the FSW process, distinct welding zones are formed due to the deformation

experienced by the processed material and to the different thermal cycles that occur during the process. In the FSWelded alloys, as the 2098-T351 Al-Cu-Li, the stir zone (SZ) is characterized by plastic deformation and intense heating that cause dynamic recrystallization [22]. This zone also presents phase dissolution and equiaxed grain shapes. In the thermo-mechanically affected zone (TMAZ), the high temperatures reached and the effect of tool movement cause the deformation of the grains [22]. Dissolution of strengthening phases also occurs in this zone [22,46]. On the other hand, no grain shape modifications in relation to the pattern material (PM) are observed in the heat affected zone (HAZ). However, the temperatures reached in this zone are reported responsible for phase dissolution and coarsening [22]. It was shown that the temperatures reached in the welding joint (TMAZ and SZ) of the FSW 2098-T351 alloy were higher (namely, 300-600 °C) in comparison to the HAZ (<380 °C) [22]. In the SZ, the high temperatures reached cause dissolution of T1 particles and the precipitation of Cu-rich particles [22]. These are the prevailing phases in over-aged tempers of Al-Cu-Li alloys [47,48]. The presence of Cu-rich particles in the different welding zones of Al-Cu-Li alloys, and the dissolution of the T1 phase, have been reported [10,12].

#### Figure 1

Figure 2 shows the Vickers microhardness profile determined across the top surface of the FSWelded 2098-T351 alloy. A conventional “W”-shaped hardness profile was obtained [7,22]. The microhardness values obtained in the PM amounted ca. 140 HV<sub>0.3</sub>, whereas in the HAZ(RS) and HAZ(AS) the microhardness values oscillated between 110 and 130 HV<sub>0.3</sub>. Finally, microhardness values around 100 HV<sub>0.3</sub> were found in the welding joint (WJ), SZ and TMAZ. Thus, significant differences are observed when the microhardness values of the PM and HAZ regions are compared to those of the WJ. On the basis of the optical micrographs shown in Figure 1 and the microhardness results plotted in Figure 2, it is possible to estimate the dimensions of the HAZ. Whereas the WJ has a length of 10 mm (shoulder domain), the HAZ extends about 5 mm from the welding joint interface (represented by the region at the bottom of the microhardness profile).

#### Figure 2

In the previous work by Milagre et al. [22], it was also shown that the lowest microhardness values were observed in the zones that reached the highest temperatures during the FSW process. This was due to the dissolution of the T1 phase, the main strengthening phase in Al-Cu-Li alloys [7,22]. This behavior has also been reported in other

works [11,12]. In the HAZ, the volume of the T1 phase is smaller than in the PM region, and consequently, the microhardness decreases, although it remains higher compared to WJ [7,22]. From the inspection of transmission electron microscopy (TEM) images taken from the welding zones of the 2098-T351 Al-Cu-Li alloy, Milagre et al. [22] provided. reported that T1 ( $\text{Al}_2\text{CuLi}$ ) and  $\delta'$  ( $\text{Al}_3\text{Li}$ ) phases were predominant in the PM and the HAZ regions, whereas in the welding joint (TMAZ and SZ), the  $\delta'$  ( $\text{Al}_3\text{Li}$ ) and  $\theta'$  ( $\text{Al}_2\text{Cu}$ ) phases were dominant, and the presence of T1 particles was scarce, in accordance with the microhardness profile obtained in this study.

Additionally to the presence of nano-sized particles, the 2098-T351 Al-Cu-Li alloy also presents micrometric particles as shown by SEM in [Figure 3](#). EDS maps from the PM of the alloy (see [Figure 3\(a\)](#)) and from the different zones of the FSWelded alloy are presented (cf. [Figure 3\(b\)](#) and [\(c\)](#)). The elemental maps show that the micrometric particles are mainly composed of Al, Cu and Fe in all cases.

[Figure 3](#)

### *3. 2 Visualization of corrosion activity*

[Figure 4](#) shows optical micrographs of the coupled zones of the 2098-T351 Al-Cu-Li alloy welded by FSW taken after various periods of immersion in naturally aerated 5 mmol/L NaCl solution up to 24 h. Different corrosion features were observed on the interfaces of the welding zones. The development of SLC sites was identified on the HAZ regions, whereas, on the WJ, trenching and cavities were observed instead. As it was mentioned above, the T1 phase is dissolved in the WJ during welding, whereas many of the Fe-Cu-rich micrometric particles, which were formed during the casting of the Al-alloys, remain in this region, although they might have been broken and dragged due to the tool movements, favoring the development of trenching corrosion. The attack surrounding the micrometric particles is characterized as superficial, whereas, at the SLC sites, the corrosion attack penetrates deeply in the alloy [49]. Development of SLC sites in the HAZ regions was observed, and deposition of localized corrosion products on these sites increased with time. Greater volumes of corrosion products were seen on the HAZ regions of the welded alloy compared to WJ. Additionally, corrosion products deposited on the advancing side (AS) occurred in larger amounts compared to the retreating side (RS), this effect being more notorious for the longer periods of immersion. These observations must be related to the larger density of T1 phase on the AS, as suggested by the microhardness results.

#### Figure 4

An interesting correlation between microhardness, corrosion resistance and the presence of the T1 phase across of the FSWelded 2198-T851 Al-Cu-Li alloy was reported by Donatus et al. [7]. In their study, the authors showed the presence of T1 phases in the HAZ and absence of these phases in the SZ from TEM micrographs. T1 precipitates dissolved completely in the SZ, where the peak temperature and the corrosion resistance were higher, and the microhardness values were lower compared to other zones. Thus, the lower density of the T1 phase in the welding zones changes the corrosion activity of each FSW zones. Other works have reported correlations between the onset of localized corrosion features and the microstructures in the different welded zones of FSW Al-Cu-Li alloys [19,26,27]. Corrosion activities were related to the T1 phase distribution in the different zones. Thus, the T1 phase was directly associated with the development of SLC sites on the Al-Cu-Li alloys [29,32]. For the FSWelded 2098-T351 alloy studied in this work, the corrosion activity in the distinct welded zones also exhibits a direct relationship with the T1 phase, directly related to the development of SLC sites on the welded zones presenting high microhardness values.

The development of galvanic corrosion processes along the welding can be visualized using an agar-agar test. This simple test can be applied to visualize the cathodic and anodic regions at different areas of the surfaces exposed to the agar-agar gel from the pH changes occurring in their surface as they are associated with a gel color modification, due to the use of a universal pH indicator [19,32]. Thus, the green color is related to high pH (alkaline), whereas, red/orange colors are associated with low pH (acidic). Figures 5-7 display surface images of the WJ/HAZ(RS) and the WJ/HAZ(AS) coupled welding zones for various durations of exposure to the agar-agar test. It can be observed that when the HAZ (either of the RS or the AS) zone is coupled to the WJ, an increase in pH, indicated by the green color scale, occurred on the WJ surface. Therefore, cathodic reactions are occurring on this zone. On the other hand, a localized pH decrease occurred over the HAZ regions, as indicated by the red color scales, which was more intense on the localized corrosion sites. These sites are associated with the occurrence of SLC, and strong anodic activity is observed at these locations when coupled to the WJ, as shown in Figures 6(a) and 7(c). Finally, no SLC sites could be observed in the WJ zones for the duration of the test (cf. Figures 6(b) and 7(b)).

#### Figure 5

#### Figure 6

#### Figure 7

Although galvanic coupling effects in other FSW Al-alloys have been characterized using the agar gel test [9,19,34], some controversy exists in the literature about the applicability of this test due to the hindrance to the free circulation of ions in the gel environment. In order to further investigate the cathodic and anodic regions on these welded zones from the associated pH changes in the adjacent electrolyte, localized microelectrochemical techniques would be advisable and they were employed in our work as described below.

### 3.3 X-ray photoelectron spectroscopy (XPS)

The surface chemical characterization of the WJ/HAZ(RS) and WJ/HAZ(AS) zones of the FSW 2098-T351 alloy associated with the corrosion process was performed by XPS. Figure 8 shows the high-resolution spectra for Al2p, Cu2p and Li1s recorded in these welding zones, both before and after corrosion tests for 72 h. Thus, Figure 8(a)-(c) shows the spectra recorded for the WJ and HAZ(RS) zones in the polished and corroded conditions, whereas Figure 8(d)-(f) depicts the spectra obtained for the WJ and HAZ(AS) zones in the same conditions. Two peaks for the Al2p signal were observed in Figure 8(a) for the polished surfaces (WJ/HAZ(RS)), one in the lowest binding energy region that is related to Al<sup>0</sup> (i.e., at 72.2 eV), whereas the other at the highest binding energy (75.4 eV) is related to the hydroxide/oxide layer naturally formed on the surface of the material [50,51]. In the polished condition, the Al2p signals were more intense for the HAZ(RS) region compared to WJ. The Al<sup>0</sup> signal was not detected in the HAZ(RS) zone after the corrosion test, whereas a very low-intensity signal for the element was observed in the WJ region after corrosion, as shown in Figure 8(a). Thus, the high resolution spectra (dotted curves) obtained in these surfaces show Al2p peaks around 74.0 and 74.5 eV, that are usually assigned to aluminum oxide/hydroxide [50]. After corrosion, the Al2p signals were slightly more intense for the WJ compared to the HAZ(RS) zone. On the other hand, Figure 8(d) shows more intense Al2p signals in the WJ than on the WJ/HAZ(AS) welded zones for the polished condition. Furthermore, the two peaks in the Al2p signal that were described above could be found for the polished condition. Conversely, very low-intensity signals for the Al<sup>0</sup> peak were observed in the WJ and HAZ(AS) zones after the corrosion tests. The high resolution spectra (dotted curves) obtained for these corroded zones, also showed Al2p peaks around 74.3 eV assigned to aluminum oxide/ hydroxide [50] (see Figure 8(d)).

Figure 8

Figure 8(b) shows the high resolution spectra of Cu2p recorded in the WJ and HAZ(RS) zones. Binding energies around 933.2 eV and 953.5 eV were observed for both the polished and the corroded welded zones. These peaks are related to Cu [52,53], Cu-rich remnant particles [54], and Cu oxide redeposition [55] on the alloy. After corrosion, the intensity of the Cu2p signal was considerably higher for the WJ compared to HAZ(RS) zones, indicating Cu-enrichment in this region. The Cu2p signal was also more intense in the WJ compared to HAZ(AS) after corrosion in Figure 8(e). During the welding process, the temperatures reached are sufficiently high to cause the dissolution of the T1 phase ( $\text{Al}_2\text{CuLi}$ ) and, consequently, Cu diffusion to the matrix. Moreover, the tool movement in this process breaks the micrometric-sized particles and favors its spread over the WJ surface [13], leading to an increase in the specific surface corresponding to the Cu-enriched micrometric particles. Besides, selective dissolution of second phases may eventually lead to Cu dissolution, and it can re-precipitate at the cathodic regions, and this would explain the more intense Cu2p signal on the WJ zone that is cathodic to the HAZ.

Li1s was not detected in the WJ/HAZ(RS) in the polished condition (cf. Figure 8(c)). However, one peak of Li1s was detected in the WJ region after the corrosion test, as shown by the blue dotted curve in Figure 8(c). This peak around 55.1 eV is related to lithium oxide [56]. When the polished WJ/HAZ(AS) was analyzed, a low intensity peak at 53.0 eV related to  $\text{Li}^0$  [56], was detected in the WJ, but it was not detected in the polished HAZ (Figure 8(f)). However, after corrosion, Li1s peaks around 55.1 eV were detected in both zones (WJ and HAZ(AS)), although they were more intense for the WJ compared to HAZ(AS), indicating that the thin oxide film of corrosion products, which was evenly distributed over the WJ, contains Li oxide. Modifications related to the surface composition provide potential differences between the WJ and the HAZ. Thus, differences in the electrochemical activity and pH changes over these welded zones are expected to occur, as it will be discussed later.

The polished HAZ(RS) surface showed higher intensity of Al2p and Cu2p compared to HAZ(AS) (cf. Figure 9(a) and (b)). After corrosion, the Al2p signal was more intense in the case of HAZ(RS), although the Cu2p signal in this region was significantly lower compared to HAZ(AS). Li1s was detected only in the HAZ(AS) region after corrosion as shown in Figure 9(c). Therefore, the layer of corrosion products was enriched in Al and Cu on the HAZ(RS), and it was enriched in Al, Cu and Li on the HAZ(AS), as noted by the spectra of the corroded surfaces compared to the polished conditions given in Figure 9. The corrosion process was more intense on the HAZ(AS) coupled with WJ and, consequently, greater intensity of the Cu

and Li signals was observed in this region. Due to distinct microstructural features in the HAZ of both sides of the weldment, changes in the corrosion behavior of these regions are likely to be observed.

Figure 9

#### *3.4 Local electrochemical behavior of the welded zones of the FSW 2098-T351 alloy*

The electrochemical characterization of the welded zones developed on the FSW 2098-T351 alloy were designed as to extract information from the different regions developed as result of the welding procedure as result of their specific microstructure and composition, as well as to unveil the galvanic coupling effects among the regions that were evidenced using the gel visualization tests described in Section 3.2. In this context, it is evident that local electrochemical behaviors should be characterized using spatially-resolved electrochemical techniques instead of considering the averaging measurements provided by conventional electrochemical methods. Secondly, both the dimensions of the heterogeneous regions produced by the FSW procedure and the spatial resolution of the microelectrochemical methods should be taken into account as to design the specific measurements to be performed and their relevance to describe the complete system. Thus, the width of the heterogeneous region produced by FSW extends along several millimeters as shown by the optical micrographs of Figure 1, whereas the effective spot sizes employed in scanning electrochemical microscopy (SECM) are typically 1-2 orders of magnitude smaller, whereas the scanning vibrating electrode technique (SVET) is typically employed to cover various hundreds of micrometers. As result, the local microelectrochemical studies were designed as to characterize the WJ/HAZ interface zones developed on both the advancing (AS) and the retreating sides (RS) when each of them was separately exposed to the test electrolyte as sketched in Figure 10. In this case, galvanic coupling effects between the corresponding HAZ and WJ regions could be characterized because the samples contained portions of the two zones simultaneously exposed to the test solution. Yet, the different spatial resolution of SVET and SECM imposed that the complete HAZ/WJ interface regions could only be imaged in one scan using SVET, whereas the higher spatial resolution of SECM motivated to image smaller areas effectively selected on the HAZ and the WJ zones. The latter was achieved by first imaging one of the zones, and subsequently moving the tip to the other side of the interface to image the other zone (cf. the red-colored small squares drawn on the sketch in Figure 10). On the other hand, an alternate procedure to the use of

scanning probe methods to achieve spatially-resolved electrochemical methods consists in the miniaturization of the sample, effectively exposing to the electrolyte only the small area confined by the microcell. In this way, the electrochemical response of the isolated region under investigation is obtained, because the other regions in the FSW are not exposed to the electrolyte, and therefore galvanic coupling effects are not effectively operating in that configuration (see sketch in Figure 10). Altogether, it is considered that the use of the three local electrochemical methods could provide complementary information for the characterization of the heterogeneous electrochemical activity of the WJ/HAZ(RS) and WJ/HAZ(AS) interfaces of the FSW alloy, as schematized in Figure 10.

Figure 10

#### 3.4.1 Local potentiodynamic polarization

Figure 11 shows anodic potentiodynamic polarization curves of the HAZ and WJ of the FSWelded 2098-T351 alloy obtained using an electrochemical micro-cell. As described above, this allows the local electrochemical activity of the specific zones to be evaluated in 5 mmol/L NaCl solution without any galvanic coupling between them or with any other region in the FSWeldment. More specifically, Figure 11(a) shows the anodic polarization curves measured for a sample consisting of the HAZ(RS) and the adjacent WJ zones for the retreating side of the weldment, while Figure 11(b) shows the corresponding anodic polarization curves of the HAZ(AS) compared to WJ in the advancing side. In addition, for the sake of comparison the anodic polarization curves obtained for HAZ(RS) and HAZ(AS) are plotted in the same graph in Figure 11c, after observing that the potentiodynamic curves measured for the WJ in two separate samples as sketched in Figure 10, effectively indicated practically the same electrochemical response as for the microelectrochemical cell configuration.

Figure 11

The anodic polarization curves are associated with the dissolution of the passive film. Thus, different electrochemical behaviors were observed in the different regions under consideration. In Figure 11(a) and (b), it is seen that the WJ presents nobler potentials (with  $E_{corr}$  values around -0.30 V) compared to the HAZ zones for either the RS or the AS sides, where  $E_{corr}$  values around -0.40 V were measured. Then, the potential differences between the WJ and the HAZ in both cases are approximately 100 mV. This potential difference explains the onset of a galvanic corrosion mechanism along the FSWeldment. Yet, solely on

the basis of the polarization curves measured using a microelectrochemical cell, it was not possible to identify differences in the corrosion potentials of the HAZ(RS) and HAZ(AS) according to Figure 11(c). Slightly lower current densities and a pseudo-passive behavior are observed in the WJ curves. These results suggest that the WJ is more resistant to corrosion than the HAZ, either in the RS and AS situations. Higher anodic current densities associated with a faster dissolution are related to the HAZ(AS) curve compared to the HAZ(RS). However, both HAZ(AS) and HAZ (RS) are more active compared to WJ. Examination of the surfaces after polarization curves (see [Figure 12](#)) revealed that the WJ region is more resistant to the occurrence of SLC. In the WJ, a non-severe although localized form of corrosion associated with the attack surrounding the micrometric particles was observed according to Figure 12(c). Conversely, the HAZ (either of the RS or the AS) exhibit SLC sites as shown in Figure 12(a) and (b).

#### Figure 12

The anodic currents related to SLC sites are significantly higher in comparison to those associated with micrometric particles. The contribution of the SLC sites becomes significant in the HAZ zones, contributing to the higher current densities compared to WJ. T1 phase dissolution and matrix enrichment in Li and Cu cause potential differences between the HAZ and the WJ. Cu enrichment at the WJ, as observed by XPS results (Figure 8), increases the corrosion rate at the anodic regions of the welded alloy. In a previous work by Araujo et al. [49], it was shown that the density of T1 phase increased the anodic currents associated with the localized corrosion in Al-Cu-Li alloys. Thus, the smaller amounts of T1 phase in the WJ would account for its significantly different electrochemical behavior compared to the HAZ, and the macrogalvanic coupling between the WZ and the HAZ (i.e., with higher content of T1 phase). In order to study this effect, localized scanning electrochemical probe studies were carried out in these coupled welding zones, as presented next.

#### 3.4.2 Scanning vibrating electrode technique (SVET)

Scanning vibrating electrode technique (SVET) maps acquired during immersion of the coupled welding zones in aerated 5 mmol/L NaCl solution during 3 h are displayed in [Figure 13](#). Figures 13(a) and 13(b) present SVET maps obtained for the coupled WJ/HAZ(RS) and WJ/HAZ (AS), respectively. For both situations, the corrosion activity was visible within 30 min of exposure to the test solution. In Figure 13(a), the development of SLC sites was

observed in the HAZ(RS) region of the weldment coupled with the WJ. This shows that the HAZ(RS) was more susceptible to the development of SLC sites compared to WJ. A similar behavior was observed for the HAZ(AS) interface in Figure 13(b). The SVET results show that the corrosion activity and current density were significantly higher in the HAZ compared to the WJ. Thus, in both sides of the weldment (i.e., AS and RS), the WJ was more resistant to corrosion according to the results presented in this work. The WJ was cathodic in relation to HAZ regions (in agreement with the observations in the gel visualization tests shown in Figures 5-7). In fact, previous works [19,26,27] showed the development of galvanic coupling effects when the WJ was coupled with adjacent regions of FSW Al-Cu-Li alloys. In those works, the WJ was more resistant to corrosion when coupled to its adjacent zones.

### Figure 13

In Figure 13(a), an anodic site in the WJ with smaller ionic current densities compared to the anodic sites in the HAZ(RS) was observed. On the other hand, anodic sites were not observed in the WJ of the coupled WJ/HAZ(AS) interface, showing a more efficient galvanic coupling effect between the WJ and HAZ(AS) with the protection of the cathodic areas (WJ). In general, Fe-Cu-rich particles promote trenching, and the high amount of these particles present in the WJ, as observed by the EDS maps shown in Figure 3, increase the cathodic activity in this region. Within this region, micro-galvanic coupling can occur between the Fe-Cu-enriched particles and the adjacent matrix, thus promoting the formation of anodic sites in this zone. It is known that Li-rich phases are anodic in relation to the aluminum matrix [23,32], and a Li1s signal was detected in the WJ of the RS after corrosion (cf. Figure 8(c)).

The SVET maps in Figures 13(a) and (b) show that the highest anodic currents were observed in the SLC sites. As commented earlier, these are directly associated with T1 phase density, which is higher in the HAZ (either of the AS or the RS) compared to the WJ. In the WJ, the T1 phase density is very low, as suggested by the microhardness profile given in Figure 2), in good agreement with reports in the literature [22]. Thus, although anodic processes are associated with trenching, the ionic current densities related to this corrosion mechanism are quite small compared to those related to the SLC activity.

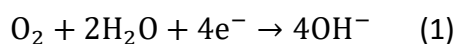
The cathodic behavior in the WJ became evident during immersion in the test solution, with a rather uniform ionic current density distribution. The predominance of cathodic activity in the WJ is due to increased amount of micrometric particles in this region that results from particles breakdown and subsequent dragging caused by the tool movement in the FSW process [13]. As noted in the XPS results in Figure 8(a) and (e), the

intensity of the Cu<sub>2p</sub> signal was considerably higher in the WJ compared to the HAZ. The high intensity of Cu in this region is related to Cu enriched micrometric particles and/or Cu redeposition at the cathodic sites. As mentioned earlier, Cu-enrichment in the WJ promotes the corrosion activity at the anodic areas, the HAZ in the case of this study, either AS or RS.

The SVET maps given in Figure 13 additionally showed that the anodic currents associated with SLC sites were larger in the HAZ(AS) compared to HAZ(RS) when these were coupled with the WJ. A similar behavior was also observed from the anodic polarization curves shown in Figure 11. Therefore, the magnitude of corrosion was different in the welded zones due to galvanic coupling. After 3 h of immersion, the corrosion activity in the SLC regions (anodic sites) of the HAZ(AS) coupled to WJ had increased with time, and higher ionic current densities were detected above them by SVET compared to the same locations for shorter periods of immersion, (see Figure 13(b)). On the other hand, in the coupled WJ/HAZ(RS) interface, the corrosion activity in the anodic sites (SLC) slightly decreased with the elapse of time according to Figure 13(a). The optical micrographs obtained in these zones, that were presented in Figure 4, support these results showing that the impact of corrosion was more intense in the HAZ(AS) compared to the HAZ(RS), when coupled to WJ. As previously mentioned, these results are explained by the differences in temperatures reached on both sides, AS and RS, during the weldment procedure, which produced different microstructural features in both sides of the weldment.

#### 3.4.3 Scanning electrochemical microscopy (SECM)

Firstly, amperometric Scanning electrochemical microscopy (SECM) measurements were performed on the coupled WJ/HAZ(RS) and WJ/HAZ(AS) interfaces of the FSWelded 2098-T351 alloy, during immersion in aerated 5 mmol/L NaCl solution. For this purpose, the amperometric Pt probe was employed using the redox competition SECM mode. In this mode, a redox-competition for the electro-reduction of dissolved oxygen in the aqueous solution occurs between cathodic regions developed in the corroding sample and the scanning probe [44]. Since oxygen is consumed by both the probe and investigated surface, a competition for this chemical species is established in the system [44,45]. The oxygen reduction reaction can be monitored by SECM under diffusion-controlled conditions according to reaction (1) by setting the potential of the Pt probe at  $-0.70$  V Ag/AgCl:



In [Figure 14](#), the SECM maps show the current distributions associated with the reduction of oxygen (i.e., oxygen consumption) between the coupled WJ and HAZ for both the RS and the AS situations. The SECM maps show the electrochemical responses related to oxygen electroreduction acquired on the coupled WJ/HAZ interfaces from locations taken on the samples as sketched in [Figure 10](#). Therefore, the upper and lower color scales in [Figure 14](#) would correspond to the different current intensities associated with oxygen consumption along the sample. Namely, the green/red/yellow colors represent the regions with greater oxygen consumption by the surface, whereas the blue color scale indicates the areas with lower oxygen depletion in the solution and therefore higher oxygen availability at the tip.

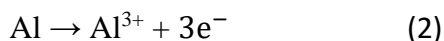
[Figure 14](#)

The measurement of smaller oxygen reduction currents at the tip were expected to occur above the WJ because more oxygen would be consumed due to greater cathodic activity when coupled with HAZ (as observed in the SVET maps shown in [Figure 13](#)). As a consequence, oxygen reduction takes place at the WJ surface. Indeed, the maps shown in [Figure 14\(a\)](#) and [\(b\)](#) show that the higher oxygen reduction currents were measured at the tip when scanning above the HAZ(RS) compared to the WJ (largest blue region), since this region presented a more anodic behavior. Thus, this observed difference occurs due to the macro-coupling between WJ and HAZ (RS). Further inspection of [Figure 14](#), allows to observe discrete locations presenting higher oxygen consumption within the HAZ(RS) (green/red colors) region. As described earlier, micro-galvanic coupling can also occur between Fe-Cu-enriched particles and the adjacent matrix. Very interestingly, Araujo et al. [49] described various localized corrosion mechanisms related to the 2198 Al-Cu-Li alloy in different temper conditions. They reported that the anodic reactions at the matrix around the micrometric particles cause Cu-enrichment in function of the preferential dissolution of Al and Li and, thus, oxygen reduction occurs on the cathodic particles. A potential difference between the matrix and the constituent particles was then shown using Volta potential maps of constituent particles in the matrix of the Al-Cu-Li alloy that were obtained by SKPFM [49]. Namely, higher potentials were recorded for the constituent particle in relation to the matrix, and these authors suggested that a galvanic coupling can occur between the constituent particle and matrix as the origin of the localized attack [49].

SECM maps of the HAZ and WJ in the case of the AS of the weldment were measured in the same way, and they are shown in [Figure 14 \(c\)](#) and [\(d\)](#). It can be observed that the

HAZ(AS) presented larger areas of oxygen consumption by the surface (i.e., red, yellow and green colored regions) compared to the HAZ(RS) (cf. Figure 14(a)). In agreement with results obtained using the other localized electrochemical methods above, the electrochemical activity of the HAZ(AS) was higher compared to HAZ(RS). Since the high temperatures reached on this side of the weldment favor greater dissolution of the T1 phase [22], the most active elements of the T1 phase (Al and Li) are preferentially dissolved and, consequently, Cu becomes enriched in this region and operate as efficient cathodes for oxygen reduction. However, despite this localized behavior, in general, when considering the complete galvanic macro-coupling among HAZ(AS), HAZ(RS) and WJ, WJ will preferentially act as the cathode (greater oxygen consumption by the surface) and the HAZ at either sides will act as an anode (greater oxygen availability at the tip).

Secondly, potentiometric SECM operation using a Sb/Sb<sub>2</sub>O<sub>3</sub> tip allowed to image the spatially-resolved pH distributions arising around the same coupled welded zones interfaces of the FSWelded 2098-T351 alloy during immersion in naturally-aerated 5 mmol/L NaCl solution, and they are shown in Figure 15. In aerated solutions at neutral or alkaline pH, oxygen reduction is the main cathodic process, according to reaction (1). As observed, oxygen reduction leads to a local alkalinization at the cathodic regions. On the other hand, at the anodic sites, the main reactions are related to metal dissolution, as given by:



In Figure 15, the blue/green color scale corresponds to regions with higher pH whereas the red scale color is related to the sites with lower pH. Local acidification was observed above the HAZ, mainly associated with the regions related to SLC sites, whereas alkalinization occurred above the corroding WJ. As it was shown by the SVET maps in Figure 13, the highest anodic currents were observed at the SLC sites present in the HAZ. In the corrosion process, the oxidation of Al to Al<sup>3+</sup> (according to reaction (2)) happens in the anodic regions. In addition, hydrogen is released due to the hydrolysis of the dissolved metal ions; consequently, a significant pH decrease will occur inside the corroding pit, leading to the observation of local acidification in the electrolyte adjacent to the SLC regions. The corrosion process at these sites is autocatalytic favoring the continuous generation of H<sup>+</sup>. On the other hand, in the WJ, it was observed that this region is not susceptible to the development of SLC sites and the attack in this zone is mainly associated with the presence of micrometric particles (cf. Figure 4). These cathodic particles that are uniformly distributed in the WJ region in addition to the dissolution of the T1 phase, account for the high cathodic

activity observed in this region. As result, higher pH values were observed in this zone. On the other hand, the regions with lower pH observed in Figure 15 are directly associated with the SLC process. They were clearly observable in both HAZ regions (either from the AS or the RS sides) coupled with WJ, whereas the latter showed higher and more uniform pH distributions for both coupled interfaces, thus directly related to the high cathodic activity concentrated in this region. This behavior is in agreement with the results presented and described previously using the other experimental methods employed in this work.

Figure 15

#### 4. Conclusions

The local electrochemical behavior distribution developed on the coupled welded zones, welding joint (WJ) and heated affected zone (HAZ), either at the advancing (AS) or the retreating (RS) sides, of the FSWelded 2098-T351 Al-Cu-Li alloy was investigated in the present work during exposure to a diluted chloride-containing aqueous solution. Macro-galvanic interactions between the coupled WJ/HAZ interfaces and micro-galvanic interactions within these zones were observed using a powerful combination of localized electrochemical methods. The analysis of anodic potentiodynamic polarization curves and scanning vibrating electrode technique maps showed that the HAZ, either at the AS or the RS, behaved anodic to the WJ, and they were more susceptible to development of severe localized corrosion (SLC) sites compared to WJ. In fact, the WJ was more resistant to localized corrosion than the HAZ. Furthermore, these techniques showed that the electrochemical activity of the HAZ(AS) coupled with the WJ was greater compared to that of the HAZ(RS). On the other hand, scanning electrochemical microscopy (SECM) operated in amperometric and potentiometric modes, was useful to monitor oxygen consumption related to cathodic activity and pH distribution along the coupled welded zones, respectively. SECM results showed that higher cathodic activities and, consequently, greater alkalization was observed on the WJ, that were correlated to a lower T1 phase content, compared to the HAZ (either of the AS or the RS). SECM in the potentiometric mode also showed that intense acidification occurred at the SLC sites in the HAZ. These observations correlated well with preliminary observations made using the agar-agar gel corrosion visualization test. Therefore, localized amperometric and potentiometric techniques have been shown to be very useful for providing new understanding about the galvanic coupling

effects and the local electrochemical activity of welded zones interfaces of Al-Cu-Li alloys welded by FSW.

### Acknowledgements

The work was supported by Fundação de Amparo à Pesquisa do Estado de São Paulo-FAPESP (Proc. 2013/13235-6, Proc.2018/06880-6 and Proc. 2019/11427-1), by the Spanish Ministry of Economy and Competitiveness (MINECO, Madrid, Spain) and the European Regional Development Fund (Brussels, Belgium) under grant CTQ2016-80522-P, and by the University of La Laguna under the Starting Research Activity program (*Ayudas a Nuevos Proyectos de Investigación: Iniciación a la Actividad Investigadora*). A.M.B.-A. acknowledges the ACIISI (Gobierno de Canarias, Las Palmas de Gran Canaria, Spain) for the grant Ref. TESIS2017010137.

### References

1. R.G. Buchheit, J.P. Moran, G.E. Stoner, Electrochemical behavior of the T1 (Al<sub>2</sub>CuLi) intermetallic compound and its role in localized corrosion of Al-2% Li-3% Cu alloys, *Corrosion* 50 (1994) 120–130. doi:10.5006/1.3293500.
2. R.J. Rioja, J. Liu, The evolution of Al-Li base products for aerospace and space applications, *Metallurgical and Materials Transactions A* 43 (2012) 3325–3337. doi:10.1007/s11661-012-115.
3. R.G. Buchheit, J.P. Moran, G.E. Stoner, Localized corrosion behavior of alloy 2090—The role of microstructural heterogeneity, *Corrosion* 46 (1990) 610–617. doi:10.5006/1.3585156.
4. V. Proton, J. Alexis, E. Andrieu, J. Delfosse, A. Deschamps, F. De Geuser, M.C. Lafont, C. Blanc, The influence of artificial ageing on the corrosion behaviour of a 2050 aluminium-copper-lithium alloy, *Corrosion Science* 80 (2014) 494–502. doi:10.1016/j.corsci.2013.11.060.
5. X. Zhang, B. Liu, X. Zhou, J. Wang, C. Luo, Z. Sun, Z. Tang, F. Lu, Corrosion behavior of friction stir welded 2A97 Al-Cu-Li alloy, *Corrosion* 73 (2017) 988–997. doi:10.5006/2418
6. U. Donatus, R.O. Ferreira, N.V.V. Mogili, B.V.G. de Viveiros, M.X. Milagre, I. Costa, Corrosion and anodizing behaviour of friction stir weldment of AA2198-T851 Al-Cu-Li alloy, *Materials Chemistry and Physics* 219 (2018) 493–511. doi:10.1016/j.matchemphys.2018.08.053.
7. U. Donatus, B.V.G. de Viveiros, M.C. de Alencar, R.O. Ferreira, M.X. Milagre, I. Costa, Correlation between corrosion resistance, anodic hydrogen evolution and microhardness in friction stir weldment of AA2198 alloy, *Materials Characterization* 144 (2018) 99–112. doi:10.1016/j.matchar.2018.07.004.
8. V. Proton, J. Alexis, E. Andrieu, C. Blanc, J. Delfosse, L. Lacroix, Influence of post-welding heat treatment on the corrosion behavior of a 2050-T3 aluminum-copper-lithium alloy friction stir welding joint, *Journal of The Electrochemical Society* 158 (2011) C139–C147. doi:10.1149/1.3562206.

9. M. Jariyaboon, A.J. Davenport, R. Ambat, B.J. Connolly, S.W. Williams, D.A. Price, The effect of welding parameters on the corrosion behaviour of friction stir welded AA2024-T351, *Corrosion Science* 49 (2007) 877–909. doi:10.1016/j.corsci.2006.05.038.
10. J.C. Rao, E.J. Payton, C. Somsen, K. Neuking, G. Eggeler, A. Kostka, J.F. Dos Santos, Where does the lithium go? - A study of the precipitates in the stir zone of a friction stir weld in a li-containing 2xxx series Al alloy, *Advanced Engineering Materials* 12 (2010) 298–303. doi:10.1002/adem.200900284.
11. W. Li, R. Jiang, Z. Zhang, Y. Ma, Effect of rotation speed to welding speed ratio on microstructure and mechanical behavior of friction stir welded aluminum–lithium alloy joints, *Advanced Engineering Materials* 15 (2013) 1051–1058. doi:10.1002/adem.201300147.
12. R.W. Fonda, J.F. Bingert, Precipitation and grain refinement in a 2195 Al friction stir weld, *Metallurgical and Materials Transactions A: Physical Metallurgy and Materials Science* 37 (2006) 3593–3604. doi:10.1007/s11661-006-1054-2.
13. R. Nandan, T. Debroy, H.K.D.H. Bhadeshia, Recent advances in friction stir welding – Process, weldment structure and properties, *Progress in Materials Science* 53 (2008) 980–1023. doi:10.1016/j.pmatsci.2008.05.001.
14. P.L. Threadgill, A.J. Leonard, H.R. Shercliff, P.J. Withers, Friction stir welding of aluminium alloys, *International Materials Reviews* 54 (2009) 49–93. doi:10.1179/174328009X411136.
15. K. Dudzik, Properties of advancing side of weld in joint welded by FSW, *Journal of KONES Powertrain and Transport* 21 (2014) 75–80. doi:10.5604/12314005.1133167.
16. Y. Deng, B. Peng, G. Xu, Q. Pan, Z. Yin, Stress corrosion cracking of a high-strength friction-stir-welded joint of an Al–Zn–Mg–Zr alloy containing 0.25 wt.% Sc, *Corrosion Science* 100 (2015) 52–72. doi: 10.1016/j.corsci.2015.06.031
17. F. Martins, U. Donatus, O. Maurício, P. Ramirez, G. De Viveiros, S. Lamaka, M. Zheludkevich, M. Masoumi, V. Vivier, I. Costa, H. Gomes, D. Melo, Effect of unequal levels of deformation and fragmentation on the electrochemical response of friction stir welded AA2024-T3 alloy, *Electrochimica Acta* 313 (2019) 271–281. doi: 10.1016/j.electacta.2019.04.137
18. R.S. Mishra, Z.Y. Ma, Friction stir welding and processing, *Materials Science and Engineering R: Reports* 50 (2005) 1–78. doi:10.1016/j.mser.2005.07.001.
19. M.X. Milagre, U. Donatus, N.V. Mogili, R.M.P. Silva, B.V.G. de Viveiros, V.F. Pereira, R.A. Antunes, C.S.C. Machado, J.V.S. Araujo, I. Costa, Galvanic and asymmetry effects on the local electrochemical behavior of the 2098-T351 alloy welded by friction stir welding, *Journal of Materials Science and Technology* 45 (2020) 162–175. doi:10.1016/j.jmst.2019.11.016.
20. T. Warner, Recently-developed aluminium solutions for aerospace applications, *Materials Science Forum* 519–521 (2006) 1271–1278. doi:10.4028/www.scientific.net/MSF.519-521.1271.
21. H.G. Salem, J.S. Lyons, Effect of equal channel angular extrusion on the microstructure and superplasticity of an Al-Li alloy, *Journal of Materials Engineering and Performance* 11 (2002) 384–391. doi:10.1361/105994902770343908.

22. M.X. Milagre, N. V. Mogili, U. Donatus, R.A.R. Giorjão, M. Terada, J.V.S. Araujo, C.S.C. Machado, I. Costa, On the microstructure characterization of the AA2098-T351 alloy welded by FSW, *Materials Characterization* 140 (2018) 233–246. doi:10.1016/j.matchar.2018.04.015.
23. J.F. Li, C.X. Li, Z.W. Peng, W.J. Chen, Z.Q. Zheng, Corrosion mechanism associated with T1 and T2 precipitates of Al-Cu-Li alloys in NaCl solution, *Journal of Alloys and Compounds* 460 (2008) 688–693. doi:10.1016/j.jallcom.2007.06.072.
24. J. Corral, E.A. Trillo, Y. Li, L.E. Murr, Corrosion of friction-stir welded aluminum alloys 2024 and 2195, *Journal of Materials Science Letters* 19 (2000) 2117–2122. doi:10.1023/A:1026710422951.
25. V. Proton, J. Alexis, E. Andrieu, J. Delfosse, M.C. Lafont, C. Blanc, Characterisation and understanding of the corrosion behaviour of the nugget in a 2050 aluminium alloy Friction Stir Welding joint, *Corrosion Science* 73 (2013) 130–142. doi:10.1016/j.corsci.2013.04.001.
26. C. Machado, U. Donatus, M. Xavier Milagre, N. Mogili, R. Giorjão, R. Klumpp, J.V. Araujo, R. Ferreira, I. Costa, Correlating the modes of corrosion with microstructure in friction stir welded AA2198-T8 alloy in aqueous hydrogen peroxide-chloride medium, *Corrosion* 75 (2019) 628–640. doi:10.5006/3054.
27. U. Donatus, R.M.P. da Silva, J.V.S. Araujo, M.X. Milagre, C.P. de Abreu, C.S.C. Machado, I. Costa, Macro and microgalvanic interactions in friction stir weldment of AA2198-T851 alloy, *Journal of Materials Research and Technology* 8 (2019) 6209–6222. doi:10.1016/j.jmrt.2019.10.015.
28. E. Ghanbari, A. Saatchi, X. Lei, D. Kovalov, D.D. Macdonald, Passivity breakdown and pitting corrosion of Al-Li aerospace alloys, 2017 Department of Defense (DoD) - Allied Nations Technical Corrosion Conference (2017) 1–15.
29. M.X. Milagre, U. Donatus, C.S.C. Machado, J.V.S. Araujo, R.M.P. da Silva, B.V.G. de Viveiros, A. Astarita, I. Costa, Comparison of the corrosion resistance of an Al-Cu alloy and an Al-Cu-Li alloy, *Corrosion Engineering, Science and Technology* 54 (2019) 402–412. doi:10.1080/1478422X.2019.1605472.
30. R.M.P. da Silva, M.X. Milagre, L.A. de Oliveira, U. Donatus, R.A. Antunes, I. Costa, The local electrochemical behavior of the AA2098-T351 and surface preparation effects investigated by scanning electrochemical microscopy, *Surface and Interface Analysis* 51 (2019) 982–992. doi:10.1002/sia.6682.
31. M.X. Milagre, U. Donatus, C.S.C. Machado, J. Victor, S. Araujo, R.O. Ferreira, R. Maria, P. Silva, R.A. Antunes, Exfoliation corrosion susceptibility in the zones of friction stir welded AA2098-T351, *Journal of Materials Research and Technology* 8 (2019) 1–14. doi:10.1016/j.jmrt.2019.09.066.
32. J.V.S. Araujo, U. Donatus, F.M. Queiroz, M. Terada, M.X. Milagre, M.C. de Alencar, I. Costa, On the severe localized corrosion susceptibility of the AA2198-T851 alloy, *Corrosion Science* 133 (2018) 132–140. doi:10.1016/j.corsci.2018.01.028.
33. J.C.B. Bertencello, S.M. Manhabosco, L.F.P. Dick, Corrosion study of the friction stir lap joint of AA7050-T76511 on AA2024-T3 using the scanning vibrating electrode technique, *Corrosion Science* 94 (2015) 359–367. doi:10.1016/j.corsci.2015.02.029.
34. C.P. de Abreu, I. Costa, H.G. de Melo, N. Pébère, B. Tribollet, V. Vivier, Multiscale

- Electrochemical study of welded Al alloys joined by friction stir welding, *Journal of The Electrochemical Society* 164 (2017) C735-C746. doi:10.1149/2.0391713jes.
35. D. Sidane, E. Bousquet, O. Devos, M. Puiggali, M. Touzet, V. Vivier, Local electrochemical study of friction stir welded aluminum alloy assembly, *Journal of Electroanalytical Chemistry* 737 (2014) 206–211. doi:10.1016/j.jelechem.2014.06.025.
  36. J.C. Seegmiller, D.A. Buttry, A SECM study of heterogeneous redox activity at AA2024 surfaces, *Journal of The Electrochemical Society* 150 (2003) B413-B418. doi:10.1149/1.1593041.
  37. M.B. Jensen, A. Guerard, D.E. Tallman, G.P. Bierwagen, Studies of electron transfer at aluminum alloy surfaces by scanning electrochemical microscopy, *Journal of The Electrochemical Society* 155 (2008) C324-C332. doi:10.1149/1.2916734.
  38. H. Zhou, X. Li, C. Dong, K. Xiao, T. Li, Corrosion behavior of aluminum alloys in Na<sub>2</sub>SO<sub>4</sub> solution using the scanning electrochemical microscopy technique, *International Journal of Minerals, Metallurgy and Materials* 16 (2009) 84–88. doi:10.1016/S1674-4799(09)60014-5.
  39. D.J. Carbonell, A. García-Casas, J. Izquierdo, R.M. Souto, J.C. Galván, A. Jiménez-Morales, Scanning electrochemical microscopy characterization of sol-gel coatings applied on AA2024-T3 substrate for corrosion protection, *Corrosion Science* 111 (2016) 625–636. doi:10.1016/j.corsci.2016.06.002.
  40. E. Tada, S. Satoh, H. Kaneko, The spatial distribution of Zn<sup>2+</sup> during galvanic corrosion of a Zn/steel couple, *Electrochimica Acta* 49 (2004) 2279–2285. doi:10.1016/j.electacta.2004.01.008.
  41. J. Izquierdo, L. Nagy, Á. Varga, J.J. Santana, G. Nagy, R.M. Souto, Spatially resolved measurement of electrochemical activity and pH distributions in corrosion processes by scanning electrochemical microscopy using antimony microelectrode tips, *Electrochimica Acta* 56 (2011) 8846–8850. doi:10.1016/j.electacta.2011.07.076.
  42. R.M. Souto, J. Izquierdo, J.J. Santana, A. Kiss, L. Nagy, G. Nagy, Progress in scanning electrochemical microscopy by coupling potentiometric and amperometric measurement modes, in: *“Current Microscopy Contributions to Advances in Science and Technology”*. Volumen 2. A. Méndez-Vilas (editor). Formatex Research Center, Badajoz (Spain), 2012, pp. 1407-1415.
  43. V.A. Nazarov, M.G. Taryba, E.A. Zdrachek, K.A. Andronchyk, V.V. Egorov, S.V. Lamaka, Sodium- and chloride-selective microelectrodes optimized for corrosion studies, *Journal of Electroanalytical Chemistry* 706 (2013) 13–24. doi: 10.1016/j.jelechem.2013.07.034.
  44. A.C. Bastos, A.M. Simões, S. González, Y. González-García, R.M. Souto, Imaging concentration profiles of redox-active species in open-circuit corrosion processes with the scanning electrochemical microscope, *Electrochemistry Communications* 6 (2004) 1212–1215. doi:10.1016/j.elecom.2004.09.022.
  45. R.M. Souto, L. Fernández-Mérida, S. González, SECM imaging of interfacial processes in defective organic coatings applied on metallic substrates using oxygen as redox mediator, *Electroanalysis* 21 (2009) 2640–2646. doi:10.1002/elan.200900232.
  46. A.K. Shukla, W.A. Baeslack, Study of microstructural evolution in friction-stir welded thin-sheet Al-Cu-Li alloy using transmission-electron microscopy, *Scripta Materialia* 56 (2007) 513–516. doi:10.1016/j.scriptamat.2006.11.028.

47. Y.S. Lee, Microstructures in over-aged Al-Cu-Li-Mg-Ag alloys, *Journal of Materials Science Letters* 17 (1998) 1161–1164. doi:10.1023/A:1006500601447.
48. P. Cavaliere, M. Cabibbo, F. Panella, A. Squillace, 2198 Al-Li plates joined by friction stir welding: mechanical and microstructural behavior, *Materials and Design* 30 (2009) 3622–3631. doi: 10.1016/j.matdes.2009.02.021.
49. J.V.S. Araujo, A.F.S. Bugarin, U. Donatus, C.S.C. Machado, F.M. Queiroz, M. Terada, A. Astarita, I. Costa, Thermomechanical treatment and corrosion resistance correlation in the AA2198 Al-Cu-Li alloy, *Corrosion Engineering, Science and Technology* 54 (2019) 575–586. doi:10.1080/1478422X.2019.1637077.
50. A. Uhart, J.C. Dupin, J.P. Bonino, D. Gonbeau, J. Esteban, J.B. Ledeuil, F. Ansart, An Auger and XPS survey of cerium active corrosion protection for AA2024-T3 aluminum alloy, *Applied Surface Science* 390 (2016) 751–759. doi:10.1016/j.apsusc.2016.08.170.
51. L. Jinlong, L. Hongyun, L. Tongxiang, Investigation of microstructure and corrosion behavior of burnished aluminum alloy by TEM, EWF, XPS and EIS techniques, *Materials Research Bulletin* 83 (2016) 148–154. doi:10.1016/j.materresbull.2016.05.013.
52. P. Campestrini, H. Terry, A. Hovestad, J.H.W. de Wit, Formation of a cerium-based conversion coating on AA2024: relationship with the microstructure, *Surface and Coatings Technology* 176 (2004) 365–381. doi: 10.1016/S0257-8972(03)00743-6
53. R. Grilli, M.A. Baker, J.E. Castle, B. Dunn, J.F. Watts, Localized corrosion of a 2219 aluminium alloy exposed to a 3.5% NaCl solution, *Corrosion Science* 52 (2010) 2855–2866. doi:10.1016/j.corsci.2010.04.035.
54. S.A. Kulinich, A.S. Akhtar, P.C. Wong, K.C. Wong, K.A.R. Mitchell, Growth of permanganate conversion coating on 2024-Al alloy, *Thin Solid Films* 515 (2007) 8386–8392. doi:10.1016/j.tsf.2007.04.164.
55. R. Viroulaud, J. Światowska, A. Seyeux, S. Zanna, J. Tardelli, P. Marcus, Influence of surface pretreatments on the quality of trivalent chromium process coatings on aluminum alloy, *Applied Surface Science* 423 (2017) 927–938. doi:10.1016/j.apsusc.2017.06.246.
56. L. Suo, Y. Hu, H. Li, M. Armand, L. Chen, A new class of solvent-in-salt electrolyte for high-energy rechargeable metallic lithium batteries, *Nature Communications* 4 (2013) 1481. doi:10.1038/ncomms2513.

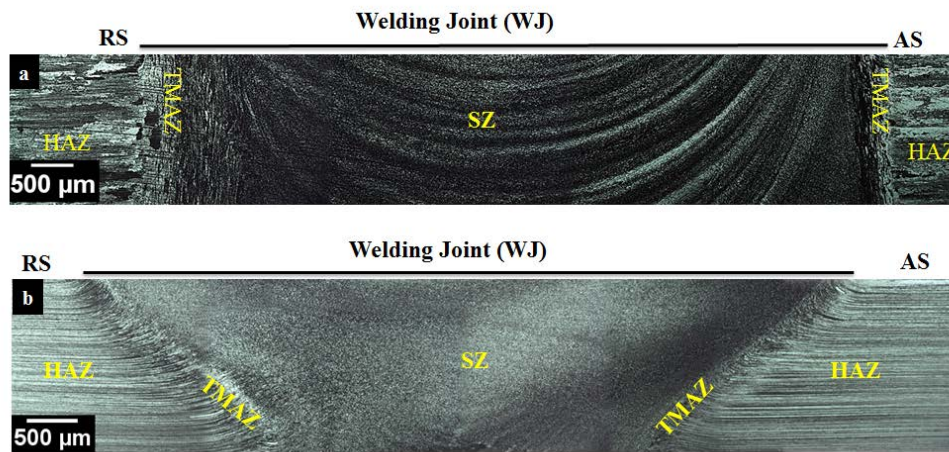


**Figure 1.** Optical micrographs of the (a) top surface and (b) cross-section of the 2098-T351 Al-Cu-Li alloy welded by FSW showing the welding zones at the retreating side (RS) and advancing side (AS).

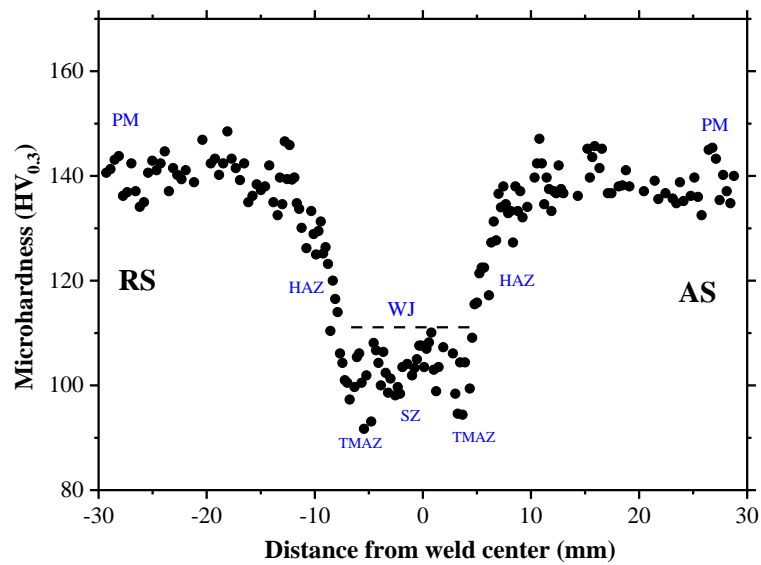


**Figure 2.** Microhardness profile of the top surface of 2098-T351 Al-Cu-Li alloy welded by FSW.

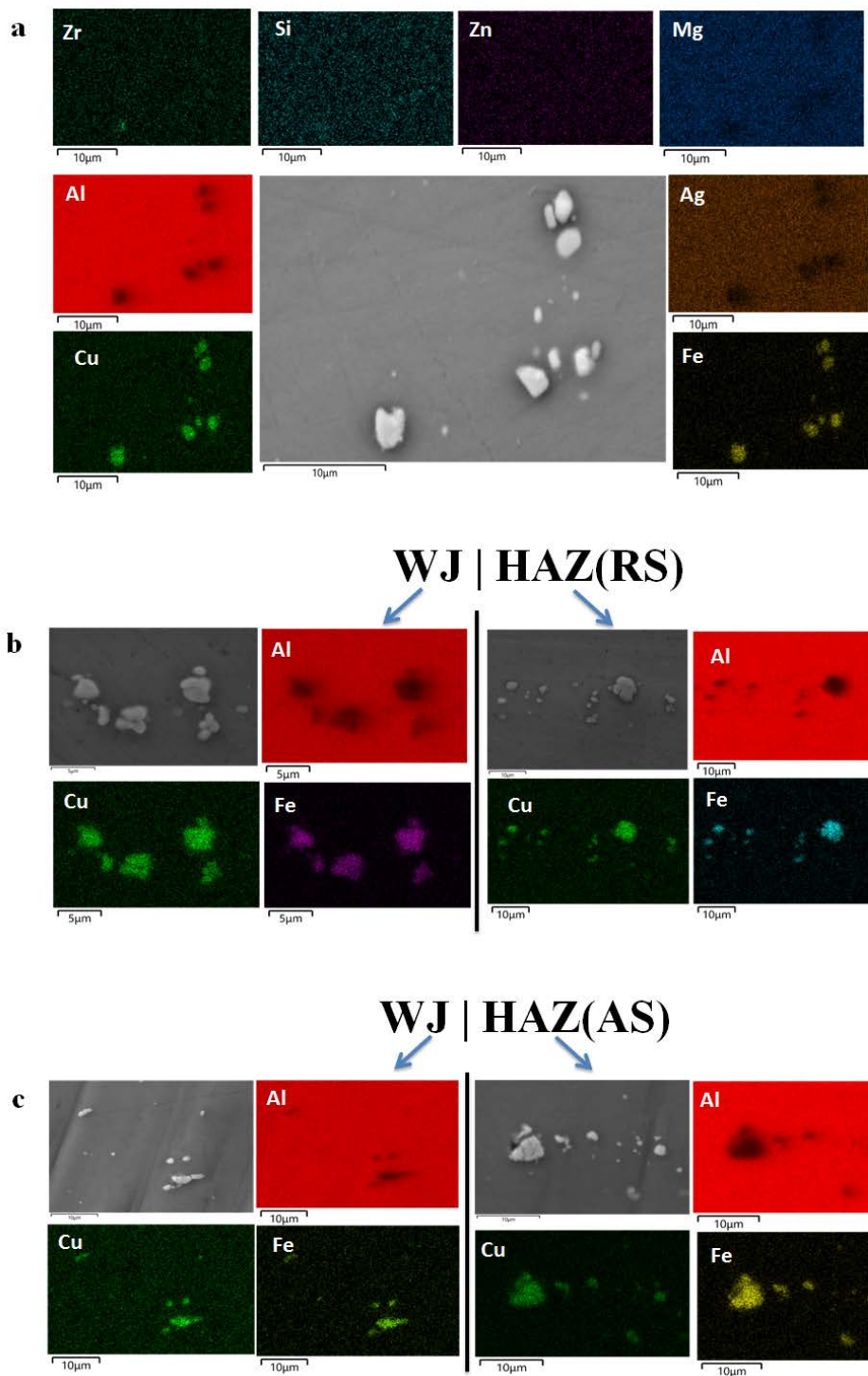


**Figure 3.** EDS maps of the micrometric particles observed in the surface of 2098-T35 Al-Cu-Li alloy: (a) parent material (PM), and in the different zones of the FSWelded alloy: (b) WJ/HAZ of the retreating side (RS), and (c) WJ/HAZ of the advancing side (AS).

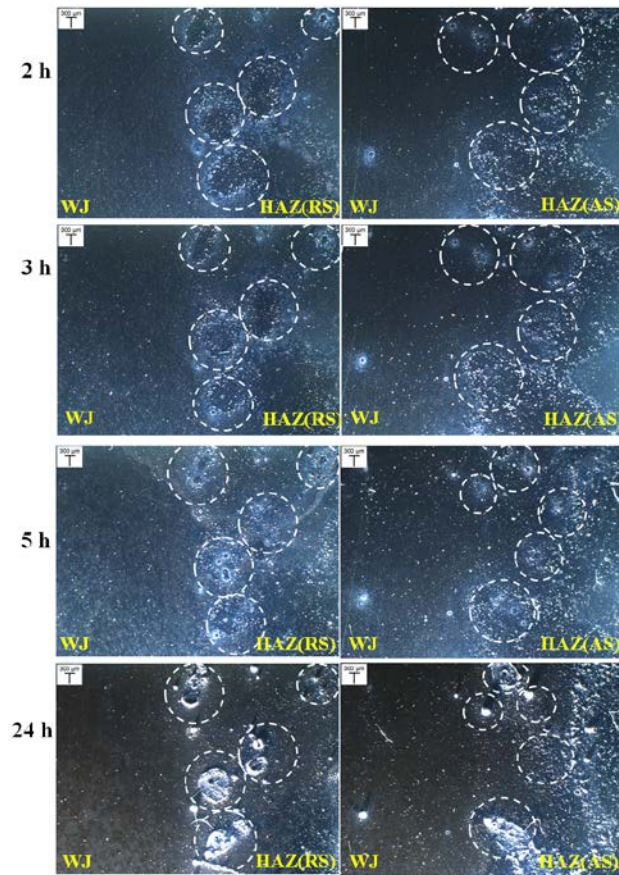


**Figure 4.** Optical images of the coupled welded zones of the 2098-T351 Al-Cu-Li alloy welded by FSW after various immersion times in aerated 5 mmol/L NaCl solution up to 24 h. White circles indicate SLC regions developed on the HAZ.

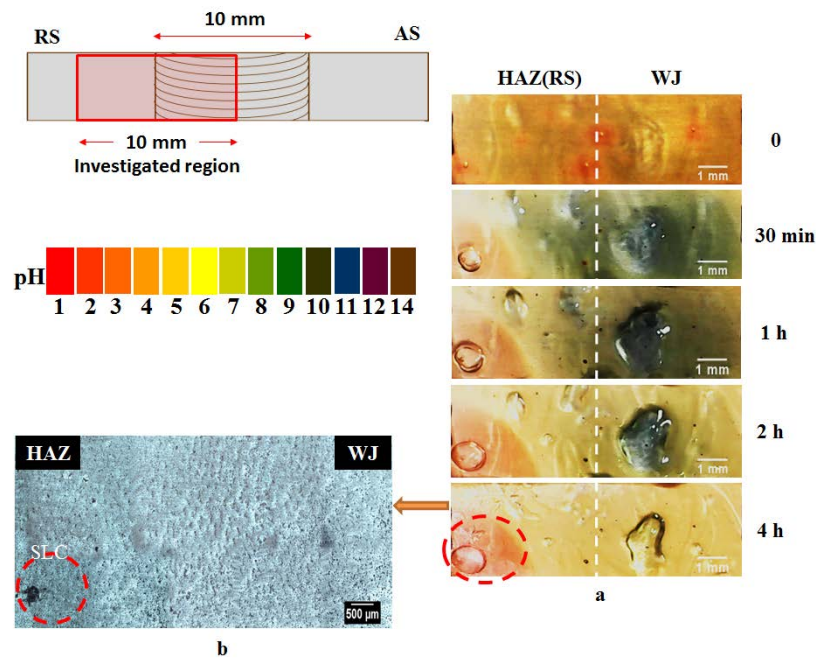


**Figure 5.** Agar visualization test of the coupled welding zones WJ/HAZ of the retreating side (RS) of the 2098-T351 Al-Cu-Li alloy welded by FSW. (a) Images obtained after various exposure times as indicated. (b) Optical image acquired after the agar test was completed.

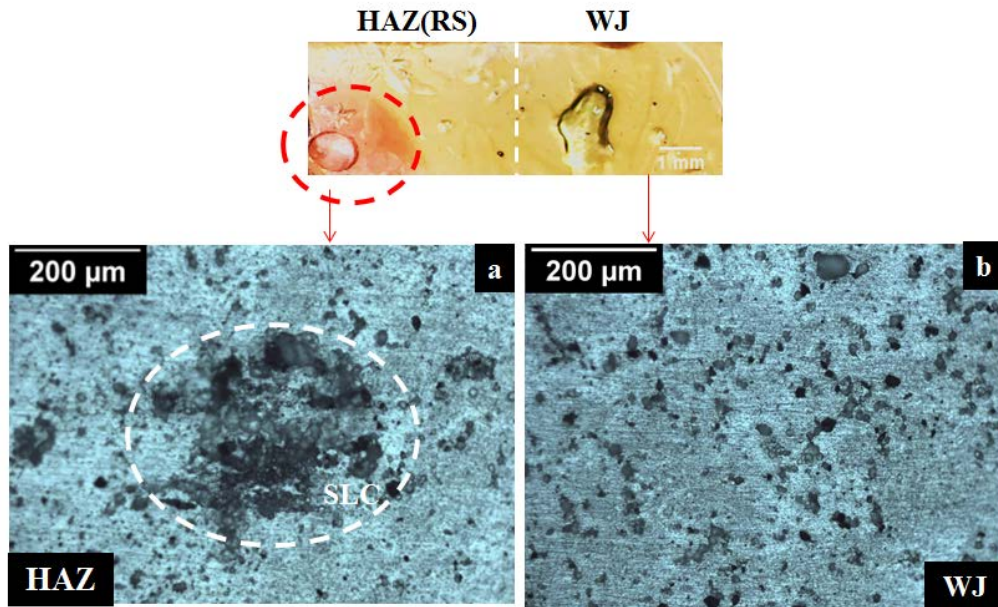


**Figure 6.** Optical images of the coupled welding zones WJ/HAZ of the retreating side (RS) acquired after the agar visualization test. White circle indicates the SLC region developed on the HAZ.

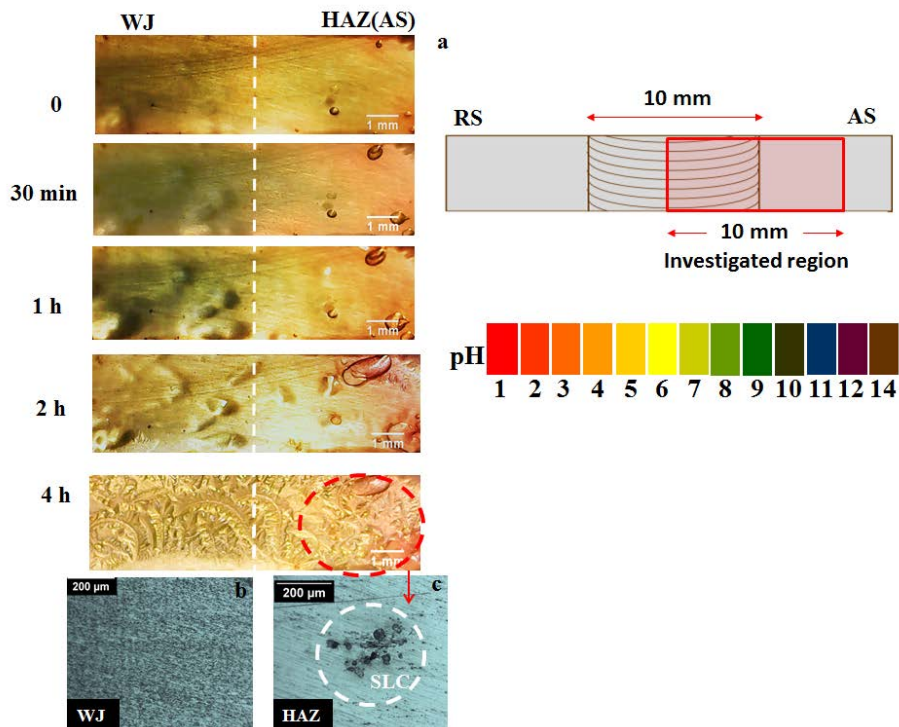


**Figure 7.** Agar visualization test of the coupled welding zones WJ/HAZ of the advancing side (AS) of the 2098-T351 Al-Cu-Li alloy welded by FSW. (a) Images obtained after various exposure times as indicated. Optical images of: (b) the WJ and (c) HAZ acquired after the test was completed.

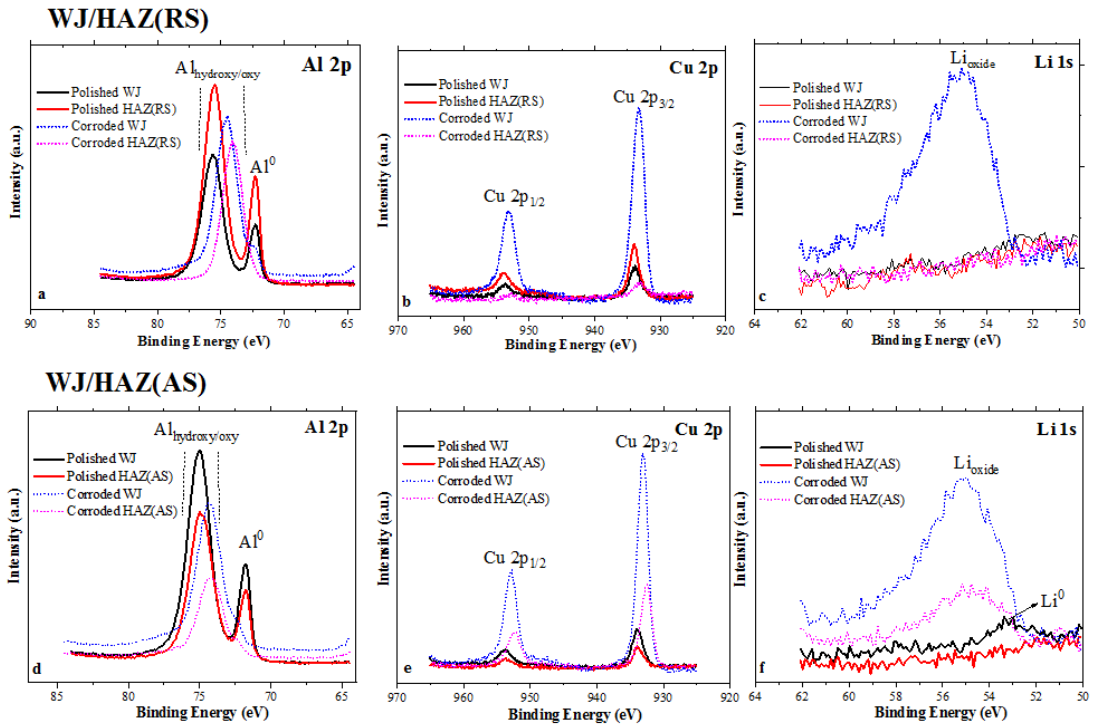


**Figure 8.** High-resolution XPS spectra of Al, Cu and Li obtained in the welding zones of the 2098-T351 Al-Cu-Li alloy welded by FSW in the polished and corroded conditions. (a)-(c) spectra obtained in the WJ/HAZ of the retreating side (RS). (d)-(f) spectra obtained in the WJ/HAZ of the advancing side (AS).

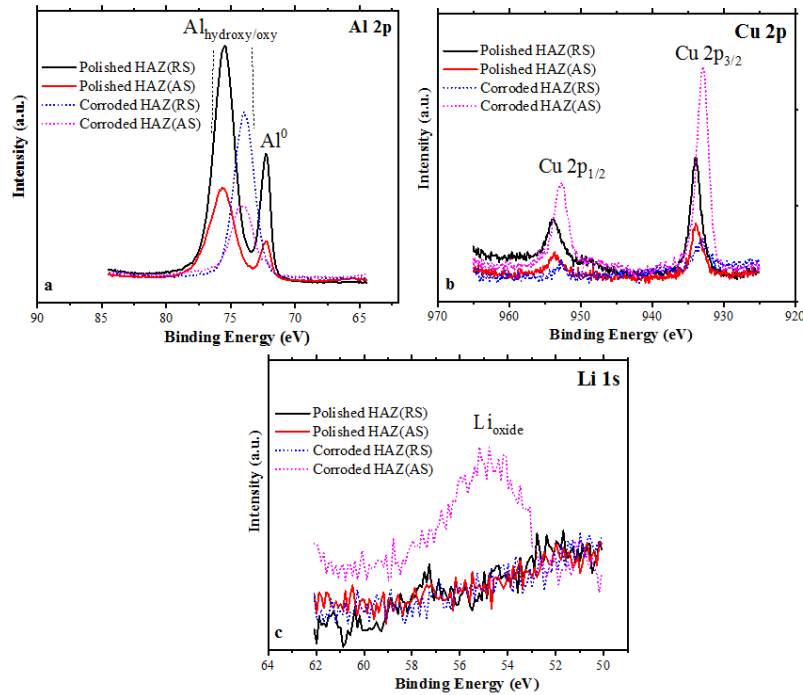


**Figure 9.** High-resolution XPS spectra of (a) Al, (b) Cu and (c) Li obtained in the HAZ of the 2098-T351 Al-Cu-Li alloy welded by FSW in the polished and corroded conditions.

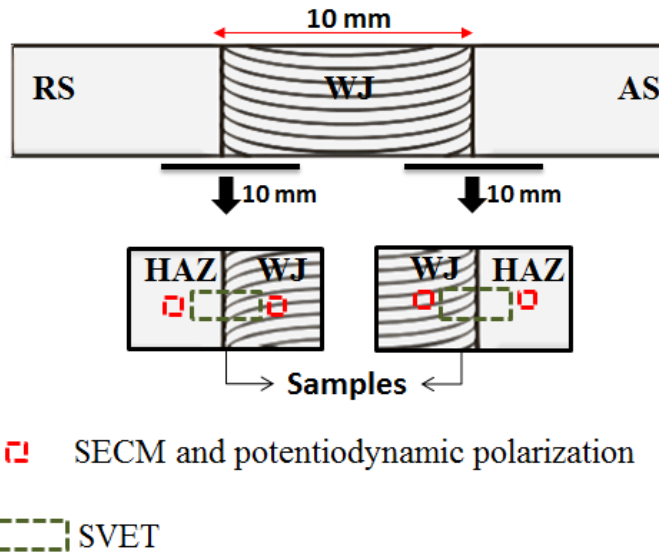


**Figure 10.** Sketch of the 2098-T351 welded by FSW showing the regions (red and green rectangles) actually sampled during the local electrochemical studies.

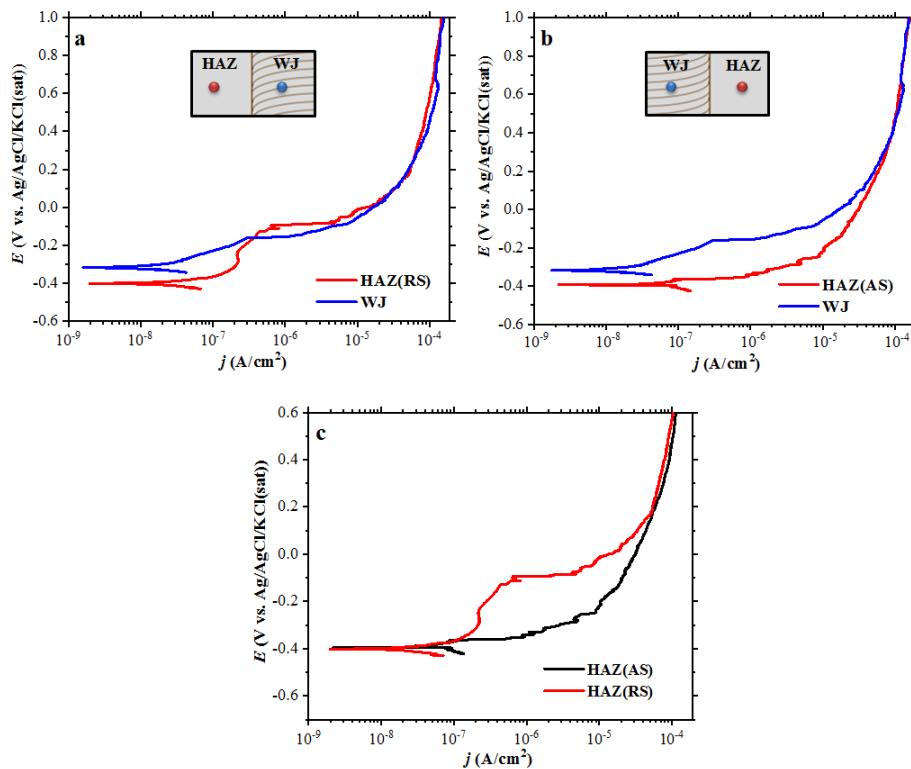


**Figure 11.** Anodic potentiodynamic polarization curves of the HAZ and WJ of the 2098-T351 Al-Cu-Li alloy welded by FSW recorded in aerated 5 mmol/L NaCl solution. (a) Curves obtained in the coupled welded zones WJ/HAZ of the retreating side (RS), (b) curves obtained in the coupled welded zones WJ/HAZ of the advancing side (AS), and (c) curves obtained in the HAZ (RS and AS) in the same previous condition assembled together for easier comparison.

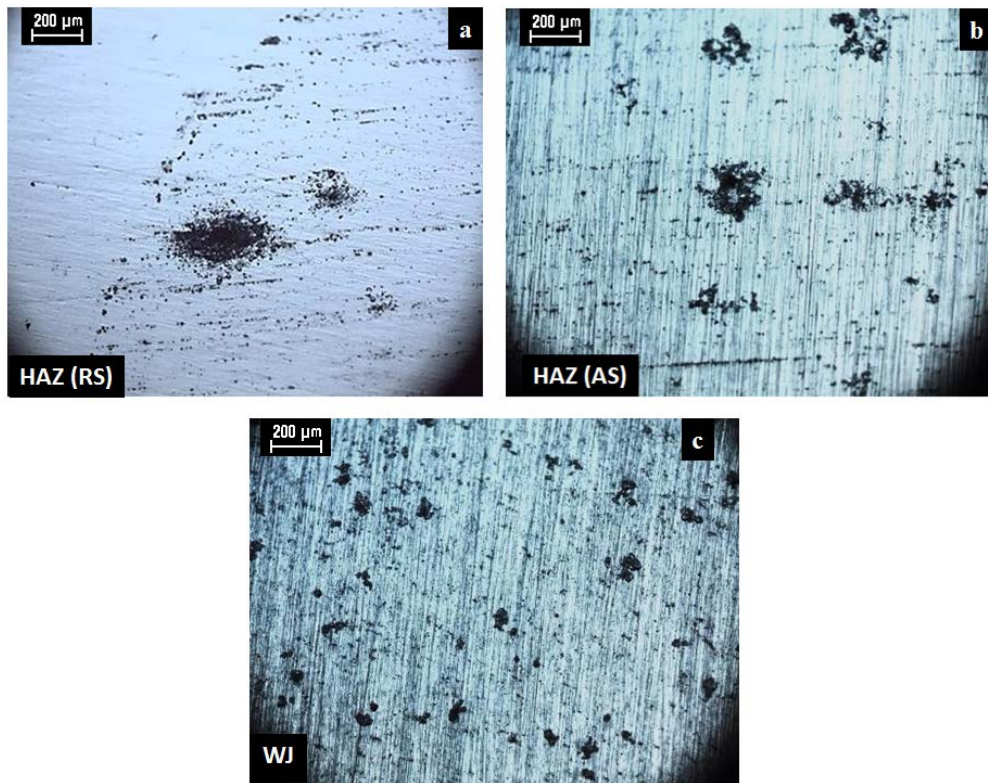


**Figure 12.** Optical images of the welded zones of the 2098-T351 Al-Cu-Li alloy welded by FSW after anodic potentiodynamic polarization.

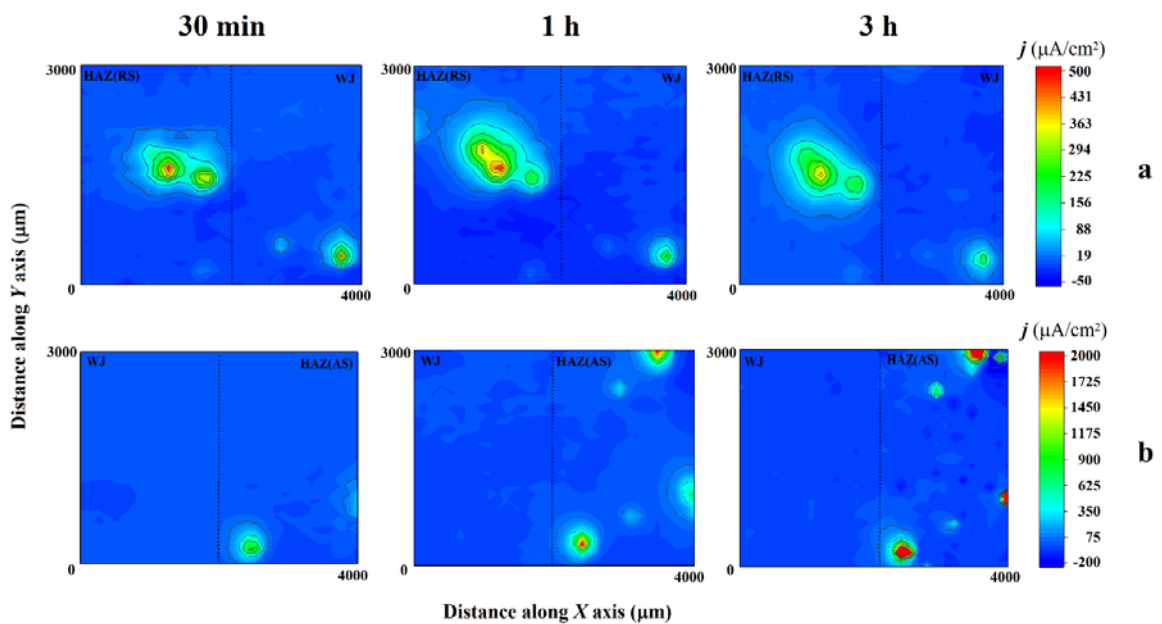


**Figure 13.** SVET maps of the HAZ/WJ regions of the 2098-T351 Al-Cu-Li alloy welded by FSW obtained in aerated 5 mmol/L NaCl solution for different periods of immersion as indicated. (a) SVET maps obtained in the coupled welded zones WJ/HAZ of the retreating side (RS), and (b) SVET maps obtained in the coupled welded zones WJ/HAZ of the advancing side (AS).

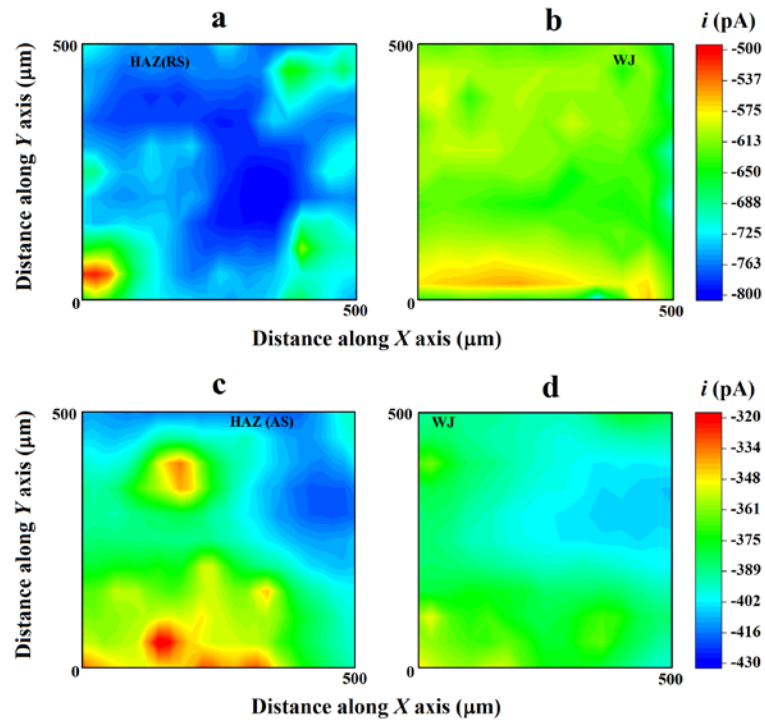


**Figure 14.** Amperometric SECM maps obtained in the coupled welded zones WJ/HAZ of the (a,b) retreating side (RS) and (c,d) advancing side (AS) of the 2098-T351 Al-Cu-Li alloy welded by FSW. They were recorded after approximately 3 h of immersion in aerated 5 mmol/L NaCl solution. Tip: Pt microelectrode biased at -0.70 V; tip-substrate distance: 20 μm; scan rate: 50 μm/s.

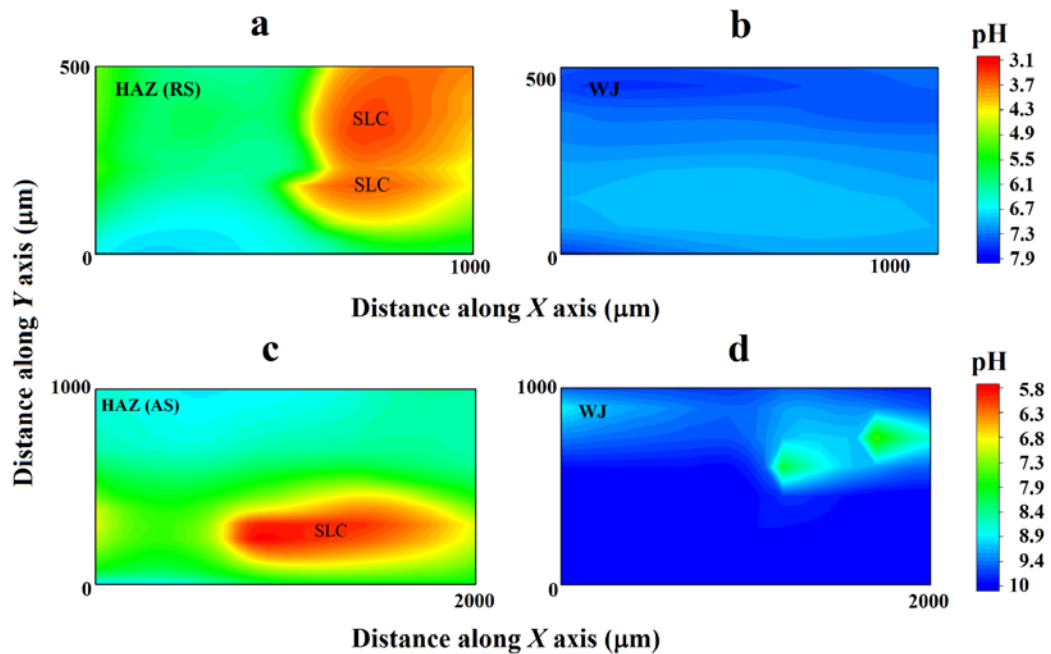


**Figure 15.** Potentiometric SECM maps obtained in the coupled welding zones WJ/HAZ of (a,b) the retreating side (RS) and (c,d) advancing side (AS) of the 2098-T351 Al-Cu-Li alloy welded by FSW after approximately 3 h of immersion in aerated 5 mmol/L NaCl solution. Tip: Sb microelectrode; tip-substrate distance: 50 μm; scan rate: 80 μm/s.